Journal of
**Applied
Crystallography**

ISSN 0021-8898

Editor: **Anke R. Kaysser-Pyzalla**

Strain-profile determination in ion-implanted single crystals using generalized simulated annealing

Alexandre Boulle and Aurélien Debelle

J. Appl. Cryst. (2010). **43**, 1046–1052

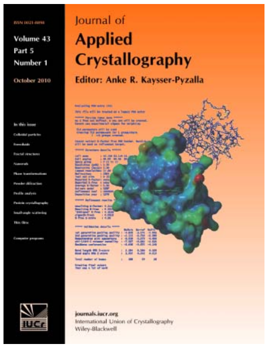

Journal of
Applied
Crystallography
ISSN 0021-8898

Received 29 March 2010
Accepted 29 July 2010

Strain-profile determination in ion-implanted single crystals using generalized simulated annealing

Alexandre Boulle[a]* and Aurélien Debelle[b]

[a]Science des Procédés Céramiques et de Traitements de Surface (SPCTS), CNRS UMR 6638, Centre Européen de la Céramique, 12 rue Atlantis, 87068 Limoges, France, and [b]Centre de Spectrométrie Nucléaire et de Spectrométrie de Masse (CSNSM, UMR 8609), CNRS – IN2P3 – Université Paris-Sud 11, Bâtiment 108, 91405 Orsay Cedex, France. Correspondence e-mail: alexandre.boulle@unilim.fr

A novel least-squares fitting procedure is presented that allows the retrieval of strain profiles in ion-implanted single crystals using high-resolution X-ray diffraction. The model is based on the dynamical theory of diffraction, including a B-spline-based description of the lattice strain. The fitting procedure relies on the generalized simulated annealing algorithm which, contrarily to most common least-squares fitting-based methods, allows the global minimum of the error function (the difference between the experimental and the calculated curves) to be found extremely quickly. It is shown that convergence can be achieved in a few hundred Monte Carlo steps, *i.e.* a few seconds. The method is model-independent and allows determination of the strain profile even without any 'guess' regarding its shape. This procedure is applied to the determination of strain profiles in Cs-implanted yttria-stabilized zirconia (YSZ). The strain and damage profiles of YSZ single crystals implanted at different ion fluences are analyzed and discussed.

1. Introduction

Zirconia is a refractory oxide that exhibits high thermal shock and corrosion resistance and good radiation stability (Kriven *et al.*, 1982). Concerning radiation stability, it has been demonstrated that cubic yttria-stabilized zirconia (YSZ) remains stable (*i.e.* it does not undergo any phase transition) upon low- and medium-energy implantation or irradiation, so that this material appears as one of the best candidates for industrial applications such as inert matrices for the transmutation of actinides (Gong *et al.*, 2000; Thomé *et al.*, 2003). In addition to radiation resistance the matrix should be able to confine radiotoxic fission products. Among these products, caesium is known to yield a significant amorphization of YSZ at high ion fluences (Wang *et al.*, 2000; Vincent *et al.*, 2008), which may jeopardize the retention properties of the matrix. The study of the structural and microstructural consequences of Cs implantation in YSZ single crystals is hence of primary importance in order to assess the qualification of this material as a matrix for the confinement of nuclear waste fuel.

In a previous work it has been shown that Cs implantation gives rise to an expansion of the YSZ unit cell in the implanted volume together with an inhomogeneous strain distribution in the direction normal to the surface (Debelle *et al.*, 2010). High-resolution X-ray diffraction (XRD) is a widely employed technique for the determination of such strain profiles, especially in the case of implanted semiconductor materials, *e.g.* Si (Diaz *et al.*, 2007; Emoto *et al.*, 2006; Hironaka *et al.*, 2000; Klappe & Fewster, 1994; Milita & Servidori, 1995; Sousbie *et al.*, 2006), SiC (Leclerc *et al.*, 2005) or GaAs (Wierzchowski *et al.*, 2005). The determination of the strain profiles from XRD data is hindered by the 'phase problem', which arises because lattice displacements affect the phase of the diffracted amplitude, E, whereas the quantity actually measured is the intensity, $I = EE^*$, so that the phase of the amplitude is lost in the diffraction experiment (Vartanyants *et al.*, 2000). Consequently, the strain profile cannot be obtained by a direct inversion of the diffracted intensity. This issue is usually circumvented by least-squares fitting a calculated XRD intensity distribution (with a parametrized strain model) to the experimental data using an appropriate minimization algorithm, such as the steepest-descent method, Newton's method (or their 'mixture', the Levenberg–Marquardt algorithm) or the simplex method (Press *et al.*, 2002; http://www.nr.com/). Common to all these methods, which are *local* optimization algorithms, is that they require a good estimate of the strain profile prior to simulation in order to avoid the algorithm being trapped in a secondary minimum. Such guess strain profiles can be obtained by complementary techniques such as Rutherford backscattering spectrometry in channeling mode (RBS/C; Debelle *et al.*, 2010), Auger electron spectroscopy (Diaz *et al.*, 2007), secondary ion mass spectroscopy (Sousbie *et al.*, 2006) or Monte Carlo simulations (Debelle *et al.*, 2010; Emoto *et al.*, 2006; Klappe & Fewster, 1994; Leclerc *et al.*, 2005; Wierzchowski *et al.*, 2005). There are cases, however, as in the present study, where the actual strain

doi:10.1107/S0021889810030281

profile significantly differs from its initial estimate, or where there is no available guess strain profile. In such a case, it is necessary to use global optimization methods that have the ability to find the global minimum regardless of the initial guess. This is the subject of the present work.

One of the most popular global optimization algorithms is simulated annealing (Kirkpatrick *et al.*, 1983), also referred to as classical simulated annealing (CSA). In this work we implement the generalized simulated annealing (GSA) algorithm (Tsallis & Stariolo, 1996) for the determination of strain profiles in Cs-implanted YSZ single crystals. As compared to CSA, which is based on the quasi-equilibrium Boltzmann–Gibbs statistics, GSA relies on Tsallis (1988) statistics, which is a generalization of the Boltzmann–Gibbs statistics. GSA has proven to be superior to CSA both in terms of its ability to accurately locate the absolute minimum of a given function and in terms of computational cost, *i.e.* convergence is reached much more rapidly (Correia *et al.*, 2005; Lemes *et al.*, 1997; Moret *et al.*, 1998; Tsallis & Stariolo, 1996; Xiang *et al.*, 1997; Zhaoxian & Dang, 2003). Despite this undeniable interest, GSA has to date not been used for the analysis of XRD data. We show in this article that GSA, combined with a cubic B-spline strain profile (Boulle *et al.*, 2003, 2009), allows one to overcome the phase problem and hence to retrieve strain profiles in a few seconds. Details concerning ion implantation and XRD data acquisition are given in §2. In §3 we present the simulation methodology, particular emphasis being laid on the description of the GSA algorithm and on its ability to rapidly converge to the global minimum. Finally, in §4, the strain profiles of Cs-implanted YSZ single crystals are discussed.

2. Experimental details

The samples used in this work are cubic (100)-oriented yttria-stabilized zirconia (9.5 mol% Y_2O_3) with fluorite-type structure and lattice parameter a = 5.145 Å. Implantations and ion-beam characterizations were performed with the JANNuS facility of the CSNSM-Orsay. Implantations were performed at room temperature with 300 keV Cs ions. An incident-beam angle of 7° was used during implantation to avoid any channeling phenomena. In the present study six crystals have been implanted with the following ion fluences: 3.75×10^{13}, 7.5×10^{13}, 3×10^{14}, 4.5×10^{14}, 6×10^{14} and 7.5×10^{14} cm^{-2}. The corresponding samples are labeled 1–6, respectively.

XRD measurements were performed in the Bragg reflection geometry on a four-circle Seifert XRD-3000 goniometer using the line focus of a copper X-ray source. A Ge(220) double-crystal monochromator (in the Cu $K\alpha_1$ setting, λ = 1.5406 Å) and a 0.1 mm primary slit were used, together with a 0.07 mm detector slit, which allowed an angular resolution of ~0.01°. A solid-state scintillation detector was used. Symmetric θ–2θ scans have been recorded in the vicinity of the (400) reflections of YSZ (2θ = 73.575°). It is emphasized that, since the strain profile is localized along the direction normal to the surface (Debelle & Declémy, 2010), the analysis of symmetric (h00) reflections is sufficient to completely determine the strain profile.

3. Simulation procedure

3.1. X-ray diffraction

In order to simulate the experimental XRD curves we calculated intensity distributions within the framework of the dynamical theory of diffraction from distorted crystals (Takagi, 1969; Taupin, 1964). The Takagi–Taupin equations describe the evolution as a function of depth (in the form of a differential equation) of the ratio of the diffracted and incident amplitude and are a function of the strain at depth z, $e(z)$, and the structure factor at depth z, $F_H(z)$ (Pietsch *et al.*, 2004).

The Takagi–Taupin equations were solved using the recursion formula of Bartels *et al.* (1986). For this purpose the implanted region of the crystal was divided into 5 nm-thick layers in which the strain $e(z)$ is constant but varies from one layer to another [according to equation (1) below]. Similarly, the structure factor in each layer is constant but is multiplied by a static Debye–Waller (DW) factor, $\exp[-L_H(z)]$, so as to take into account the effect of lattice disorder consecutive to implantation (Milita & Servidori, 1995). In a first step we assume that, in each layer, $L_H(z)$ is related to the strain according to $L_H(z) = \alpha e(z)^2$ (Sousbie *et al.*, 2006), where α is a fitting parameter. This assumption is further discussed in §4.

In the following, we assume that the strain profile, $e(z)$, can be correctly described by a cubic spline function, so that we can make use of the cubic B-spline representation

$$e(z) = \sum_{i=1}^{N} w_i B_{i,3}(z), \tag{1}$$

where w_i is the weight at knot i of the B-spline of third degree, $B_{i,3}(z)$, and N is the number of knots chosen to compute $e(z)$ (Boulle *et al.*, 2003). Hence, given a discrete set of w_i, we are able to generate the complete $e(z)$ profile by means of equation (1). The degree of detail that can be rendered entirely depends on the number of knots. Keeping the number of knots as low as possible results in a significant smoothing of the strain profile, with the risk of wiping out small details. Conversely, increasing the number of knots increases the ability to render tiny features of $e(z)$, but at the same time it increases the possibility for $e(z)$ to exhibit wild oscillations during the simulation procedure. Note that if N knots are used, the strain profile is actually divided into $N - 3$ equally sized regions. More details and a discussion concerning the advantages of using cubic B-splines can be found elsewhere (Boulle *et al.*, 2003, 2009). A representation of a strain profile defined by eight basis functions is given in Fig. 1. In order to ensure a smooth transition from the implanted region to the virgin crystal, the weights of the three last B-splines (indicated by the dotted curves) are fixed to 0, so that only five fitting parameters remain. For simplicity all weights were taken to be equal to 0.5 in Fig. 1, so that, in the implanted region (ignoring the transition zone), the strain is constant and equal to 0.5%. In the present case, it turned out that five nonzero weights are sufficient for sample 1, whereas up to ten were necessary in the case of sample 6, which exhibits a more complex XRD curve.

Finally, the resolution of the diffractometer is taken into account by convolving the calculated intensity distribution with a Gaussian function whose width is adjusted so that the peak emanating from the virgin part of the crystal is correctly described. The computer program has been written using the Python (http://www.python.org/) programming language associated with the SciPy (http://www.scipy.org/) scientific library.

3.2. Generalized simulated annealing

3.2.1. Background: classical simulated annealing. The fitting of experimental data with a calculated model consists in minimizing an appropriate error function, which measures the difference between the experimental and the calculated curves. In the following we make use of the following error function (Boulle *et al.*, 2009):

$$E = \sum_{i=1}^{M} \left[\log(I_i^{\rm cal}) - \log(I_i^{\rm obs})\right]^2 / M, \tag{2}$$

where M is the number of data points and $I_i^{\rm cal}$ and $I_i^{\rm obs}$ are the calculated (as described in the previous section) and observed intensities. The values of the error function at each point of the parameter space, *i.e.* for all possible values of the parameters of the model, form a hypersurface with several maxima and minima. The goal of any optimization algorithm is to find the deepest minimum, which corresponds to the best possible agreement between the model and the experimental data. The CSA algorithm performs this minimization by randomly exploring the hypersurface using a Gaussian visiting distribution: for each computing step the vector of parameters $\mathbf{x}_t$ is updated according to $\mathbf{x}_t = \mathbf{x}_{t-1} + \Delta\mathbf{x}$, where $\Delta\mathbf{x}$ is a vector of Gaussian random variables and t is the computing time (expressed in Monte Carlo steps, MCS). If the parameter jump is downhill (the error function is lowered, $\Delta E < 0$) the new configuration is accepted and constitutes the starting point for the next jump. If the jump is uphill (the error function is increased, $\Delta E > 0$) the jump might be accepted according to an acceptance probability, which, in the case of CSA, is the Boltzmann–Gibbs acceptance probability. This gives rise to the Metropolis criterion for the uphill jump acceptance (Metropolis *et al.*, 1953):

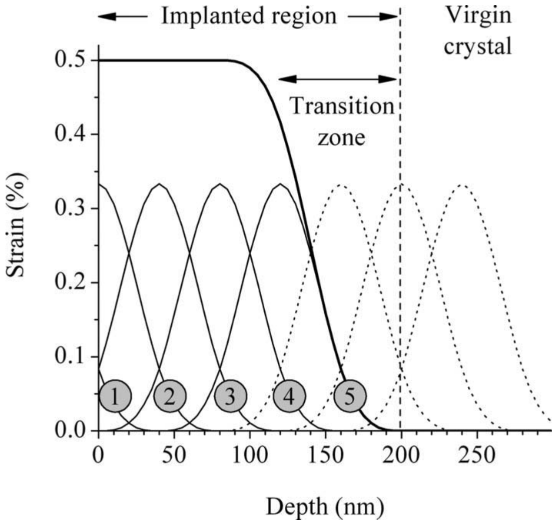

Figure 1
Example strain profile (thick black line) calculated with five nonzero basis functions (thin black lines, labeled 1–5). The weight w of each basis function was taken to be equal to 0.5. The weight of the last three basis functions (dotted curves) is fixed to 0 in order to ensure a smooth transition from the implanted region to the virgin region of the crystal.

$$r \leq \exp[-\Delta E / T(t)], \tag{3}$$

where T is an artificial temperature and r is a uniform random number lying between 0 and 1. The possibility of uphill moves allows the algorithm to detrap from local minima. With increasing time, the temperature is decreased so that the uphill jump probability decreases and the system is hopefully in the close vicinity of the global minimum (Kirkpatrick *et al.*, 1983; Tsallis & Stariolo, 1996). CSA has been successfully used in many fields of physics and chemistry, and it has been shown that this algorithm will always reach the global minimum provided that the temperature decreases logarithmically with time (Geman & Geman, 1984). However, this last property results in extremely slow convergence rates. Much effort has therefore been directed towards increasing the convergence speed without increasing the probability of being trapped in a local minimum. Along this line the most efficient algorithm, the GSA algorithm, has been proposed by Tsallis & Stariolo (1996).

3.2.2. Implementation of GSA. Within the framework of GSA we make use of the generalized thermostatistics (Tsallis, 1988) instead of the Boltzmann–Gibbs statistics, so that the Gaussian visiting distribution is replaced with

$$g_{q_{\rm v}}(\Delta x) = \left(\frac{q_{\rm v}-1}{\pi}\right)^{D/2} \frac{\Gamma\left[1/(q_{\rm v}-1)+(D-1)/2\right]}{\Gamma\left[1/(q_{\rm v}-1)-1/2\right]} \times \frac{[T(t)]^{-D/(3-q_{\rm v})}}{\left\{1+(q_{\rm v}-1)(\Delta x)^2/[T(t)]^{2/(3-q_{\rm v})}\right\}^{1/(q_{\rm v}-1)+(D-1)/2}}, \tag{4}$$

where D is the number of fitting parameters (the dimension of the vector $\mathbf{x}$), Γ is the Gamma function and $q_{\rm v} \in (1, 3)$ defines the shape of the distribution: for $q_{\rm v} \to 1$ we obtain the Gaussian distribution, $q_{\rm v} = 2$ corresponds to the Lorentzian distribution and for $q_{\rm v} > 2$ we obtain 'super-Lorentzian' distributions exhibiting tails decreasing slower than $1/\Delta x^2$ (Fig. 2). With such tails, the parameters occasionally perform very long jumps, which ensures a more efficient detrapping as compared to the Gaussian distribution and hence a faster convergence. Such long jumps are known as Lévy flights; the relationships between Lévy distributions and Tsallis statistics has been discussed by Rathie & Da Silva (2008) (see also Alemany & Zanette, 1994; Wilk & Wlodarczyk, 2000; Brouers *et al.*, 2004).

The GSA algorithm implies the generation of random numbers $\Delta\mathbf{x}$ effectively obeying equation (4), *i.e.* Tsallis random numbers (instead of Gaussian random numbers). Until recently, this was quite a difficult task. In this work we make use of the recently introduced Tsallis random number generator proposed by Schanze (2006), which produces random numbers obeying exactly equation (4):

$$\Delta\mathbf{x} = \mathbf{y}/(su^{1/2}), \tag{5a}$$

where $\mathbf{y}$ is a D-dimensional vector of Gaussian random variables, u is a random variable obeying the $\gamma\,(1, p)$ distribution, and the parameters p and s are given by

$$p = \frac{3 - q_{\rm v}}{2(q_{\rm v} - 1)} \quad \text{and} \quad s = \frac{[2(q_{\rm v} - 1)]^{1/2}}{T^{1/(3-q_{\rm v})}}. \tag{5b}$$

In implementing equation (5), we make use of the Gaussian and gamma random number generators included in the SciPy library. The exactness of equation (5) can be assessed by comparing equation (4) with a probability distribution function (p.d.f.) obtained with equation (4) (Fig. 2). It can be seen that the p.d.f. of random numbers generated with equation (5) perfectly matches the expected distribution whatever the value of the shape parameter $q_{\rm v}$.

At each computing step a new random vector $\Delta\mathbf{x}$ is generated [using equation (5)] and each parameter x_i ($i \in [1, D]$) is modified according to

$$x_{i,t} = x_{i,t-1} + k_i \Delta x_i, \tag{6}$$

where k_i is a scale factor that takes into account the fact that the different parameters may differ by several orders of magnitude. In the present case the weights w_i are of the order of unity, whereas the parameter α can be of the order of several hundreds. This modification yields a significant gain in computing efficiency by avoiding a situation in which the larger parameters evolve in very small steps.

Within the framework of GSA, the temperature cooling schedule is given by (Tsallis & Stariolo, 1996)

$$T(t) = T(0)\frac{2^{q_{\rm v}-1} - 1}{(1+t)^{q_{\rm v}-1} - 1}. \tag{7}$$

The initial temperature $T(0)$ is chosen so that the jump for each parameter remains roughly within the range of acceptable values for each parameter. Nonetheless, each time x_i exceeds the range of acceptable values, a new Δx_i is generated using equation (5). Moreover, we have found that the efficiency of the algorithm is increased if the temperature is decreased stepwise, each step lasting 100 MCS. This allows the parameter space to be sufficiently explored for each temperature.

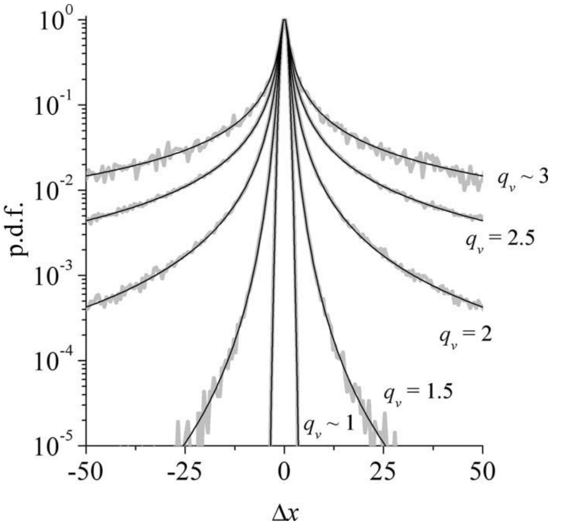

Figure 2
Probability distribution function of Tsallis random numbers with $D = 1$ and $T = 1$ for different values of $q_{\rm v}$. The theoretical p.d.f. calculated with equation (4) (thin black lines) and the experimental p.d.f. calculated from equation (5) (thick gray lines) perfectly superimpose. The experimental p.d.f. curves were computed from 106 random numbers with a histogram size of 0.5. All curves are normalized to unit maximum. Since equation (4) is not defined for $q_{\rm v} = 1$ and $q_{\rm v} = 3$, the cases $q_{\rm v} \simeq 1$ and $q_{\rm v} \simeq 3$ have actually been computed with $q_{\rm v} = 1.01$ and $q_{\rm v} = 2.99$, respectively.

Similarly to CSA, a downhill jump is always accepted. An uphill jump is accepted if the generalized Metropolis criterion is met, *i.e.*

$$r \leq \left[1 + (q_{\rm a} - 1)\Delta E/T(t)\right]^{1/(1-q_{\rm a})}, \tag{8}$$

where $q_{\rm a} \in (-\infty, 1)$ is the acceptance parameter and r is a uniform random number lying between 0 and 1. For $q_{\rm a} < 1$ the uphill probability is set to 0 when $1 + (q_{\rm a} - 1)\Delta E/T(t) < 0$ to ensure that the probability lies in the range [0, 1]. Notice that $q_{\rm v} = q_{\rm a} = 1$ corresponds to CSA, whereas $q_{\rm v} = 2q_{\rm a} = 2$ (*i.e.* a Lorentzian visiting distribution combined with the classical Metropolis criterion) corresponds to the so-called fast simulated annealing algorithm (Szu & Hartley, 1987). Earlier studies have shown that convergence is faster for $q_{\rm a} < 1$ (Penna, 1995). A significant improvement of the GSA algorithm has been implemented by Xiang *et al.* (1997). Instead of using a constant $q_{\rm a}$, they suggest to use a decreasing $q_{\rm a}$,

$$q_{\rm a}(t) = q_{\rm a}(0) - \lambda t, \tag{9}$$

where λ is a constant (0.85 in the present case). With this modification, for large computing times, the uphill acceptance probability is almost zero [equation (8)] so that GSA behaves as a steepest-descent-type algorithm. The GSA algorithm used in combination with equation (9) will hereinafter be denoted as improved GSA (iGSA). The influence of the acceptance parameter on the convergence speed is further discussed in the next section.

In brief, the GSA algorithm can be summarized as follows:

(1) Given a set of parameters [$q_{\rm v}$, $q_{\rm a}(0)$ and $T(0)$], generate a random vector of parameters $\mathbf{x}_0$. Compute the corresponding error function E_0 [equation (2)].

(2) Using equation (5), generate a random jump of parameters $\Delta\mathbf{x}$, compute $\mathbf{x}_t$ [equation (6)] and the corresponding error function E_t [equation (2)].

(3) If the jump is downhill ($E_t < E_{t-1}$), the new configuration is accepted (*i.e.* replace $\mathbf{x}_{t-1}$ by $\mathbf{x}_t$). If the jump is uphill ($E_t \geq E_{t-1}$), the new configuration is accepted only if the generalized Metropolis criterion is satisfied [equation (8)]. Otherwise, the configuration is rejected (*i.e.* keep the previous configuration $\mathbf{x}_{t-1}$).

(4) Decrease T [equation (7)] and $q_{\rm a}$ [equation (9)] and return to step (2) until the maximum number of iterations is reached, $t = t_{\max}$. The algorithm returns the parameters $\mathbf{x}_t$ corresponding to the lowest error function encountered, $E_{t,\min}$.

3.3. Performance of the algorithm

In this section the efficiency of the GSA algorithm, applied to the determination of strain profiles from XRD data, is discussed using sample 1 (corresponding to a fluence of 3.75 × 10^{13} cm^{-2}) as an example. For this sample, the implanted thickness was fixed to 200 nm (according to previous results, see Debelle *et al.*, 2010) divided into 5 nm-thick layers for the Takagi–Taupin calculation. Six fitting parameters were used: five B-spline weights and the strain/Debye–Waller proportionality constant, α. The shape parameter was fixed to $q_{\rm v} = 2.6$ and the acceptance parameter was $q_{\rm a} = -5$ [or $q_{\rm a}(0) = -5$ when using equation (9)]. Note that several ($q_{\rm a}$, $q_{\rm v}$) values have been tested in this work. We here only retain those (−5, 2.6) that gave the best results for this particular problem (this point is further discussed at the end of this section). For comparison, the results obtained with CSA ($q_{\rm v} = q_{\rm a} = 1$) are also given.

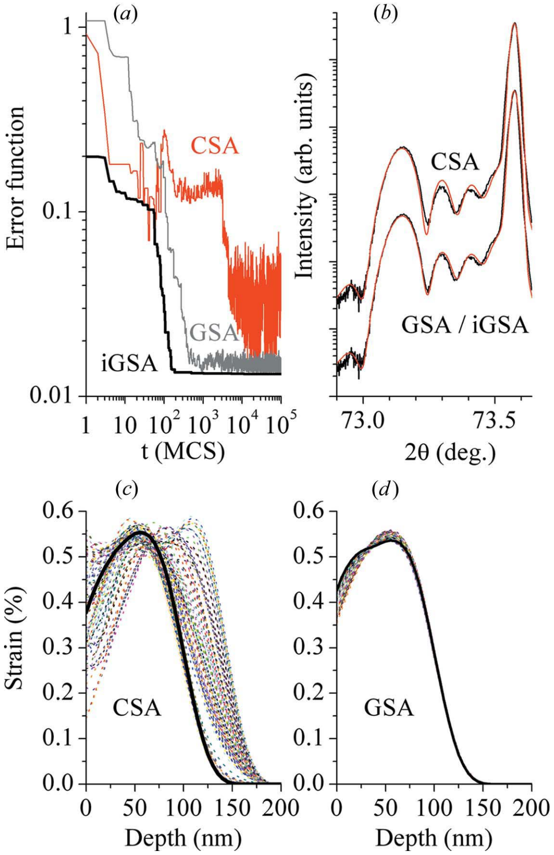

Figure 3

(*a*) Evolution of the error function for three different simulations using conventional simulated annealing (CSA, red curve), generalized simulated annealing (GSA, gray curve) and generalized simulated annealing improved with equation (9) (iGSA, black curve). GSA and improved GSA clearly outperform CSA. (*b*) Simulation of θ–2θ scans in the case of CSA (upper curve) and GSA or iGSA (both approaches yield the same result, lower curve); black line: experimental data; red line: simulation. The curves are shifted vertically for clarity. (*c*) Retrieved strain profile in the case of CSA (thick black curve). The dotted colored curves correspond to 100 profiles randomly chosen within the last 10^4 cycles so as to give an estimation of the uncertainty on the retrieved strain profile. (*d*) Retrieved strain profile in the case of GSA and iGSA (thick black curve). The dotted colored curves correspond to 100 profiles randomly chosen within the last 10^4 cycles of the GSA algorithm. It can be seen that the uncertainty is significantly reduced. In the case of iGSA the uncertainty is smaller than the line width.

The evolution of the error function [equation (2)] as a function of the computing time is reported in Fig. 3(*a*), in the case of three successful[1] fitting procedures using CSA, standard GSA and iGSA. For each algorithm several simulations were performed, and we present here the best results obtained in each case. In all cases the initial set of parameters is randomly chosen. First of all, it appears that GSA is significantly quicker than CSA: the iGSA algorithm is able to find the global minimum ($E = 0.013$) in ∼200 MCS (6 s), whereas an approximate solution ($E = 0.014$) is found with CSA in ∼20 000 MCS (10 min). The global minimum is also reached with GSA in ∼1000 MCS (30 s). Strictly speaking, in the case of CSA, convergence is not reached since the error function oscillates significantly, even for long computation times. These oscillations are due to accepted uphill moves which are mandatory to detrap from local minima, but at the same time this possibility increases the computing time. These oscillations are drastically reduced in the case of GSA, because of the negative acceptance parameter which progressively inhibits uphill moves, as shown by equation (8). As a consequence, the convergence speed is significantly increased, as mentioned earlier. This fast convergence is made possible by the long tails of the Tsallis visiting distribution (see Fig. 2 for high $q_{\rm v}$ values) so that efficient detrapping is ensured by 'tunneling' out from local minima. Finally, in the case of iGSA, there is a strict convergence in the sense that the algorithm perfectly remains within the global minimum as soon as this one is reached.

The simulations corresponding to the best solutions obtained with GSA and CSA are reported in Fig. 3(*b*): an almost perfect agreement is achieved with GSA (an identical simulation is obtained with iGSA), whereas the intensity of the fringes is not perfectly reproduced with CSA. The corresponding strain profiles are given in Figs. 3(*c*) and 3(*d*) (solid black lines). Although the overall shape is similar, there are noticeable differences in the 0–75 nm depth range. Besides, the main issue arises from the fact that in the case of CSA the error function oscillates, even for very long computing times. This makes the reliability of the obtained solution somewhat questionable. This is illustrated in Figs. 3(*c*) and 3(*d*) where 100 strain profiles (randomly chosen within the last 10^4 cycles, colored dotted curves) are plotted in order to provide an estimation of the confidence limit on the retrieved strain profile. It clearly appears that there is a huge uncertainty range in the case of CSA, whereas in the case of GSA the maximum uncertainty on the derived strain profiles is $\Delta e \simeq 0.1\%$. In the case of iGSA, since the error function remains stable, the uncertainty range is smaller than the line width.

Finally we would like to emphasize that the efficiency of GSA (as compared to CSA, for instance) and the appropriate choice of parameters [the shape parameter $q_{\rm v}$, the acceptance parameter $q_{\rm a}$, the initial temperature $T(0)$] are strongly

[1] We have here chosen a simple example with only six parameters so that all three algorithms were able to find a solution in a relatively short time. There are cases, however, especially for sample 6 for which up to 20 parameters are necessary, where CSA simply failed to find a solution in a reasonable time.

problem-dependent. Actually, significantly different behaviors have been observed for different types of problems, such as fitting ellipsometric curves (Zhaoxian & Dang, 2003) or low-energy electron diffraction patterns (Correia *et al.*, 2005), calculation of the ground-state geometry of clusters (Lemes *et al.*, 1997), electrostatics (Xiang *et al.*, 1997), and function minimization (Tsallis & Stariolo, 1996). The conclusions drawn in the present work (and in others) are hence not general and each problem requires a careful adjustment of the different parameters.

4. Results and discussion

The iGSA algorithm is now applied to the investigation of the strain depth profiles in Cs-implanted YSZ single crystals. The results of the simulations for all samples studied are given in Fig. 4(*a*), and the associated strain profiles are displayed in Fig. 4(*b*). A successful simulation has been obtained in all cases. Inspection of the retrieved strain profiles reveals that with increasing ion fluence (i) the overall width of the implanted region increases, (ii) the magnitude of the strain increases and (iii) the location of the maximum strain is shifted towards greater depths. These observations are in good qualitative agreement with transmission electron microscopy observations and RBS/C experiments (Vincent *et al.*, 2008; Debelle *et al.*, 2010).

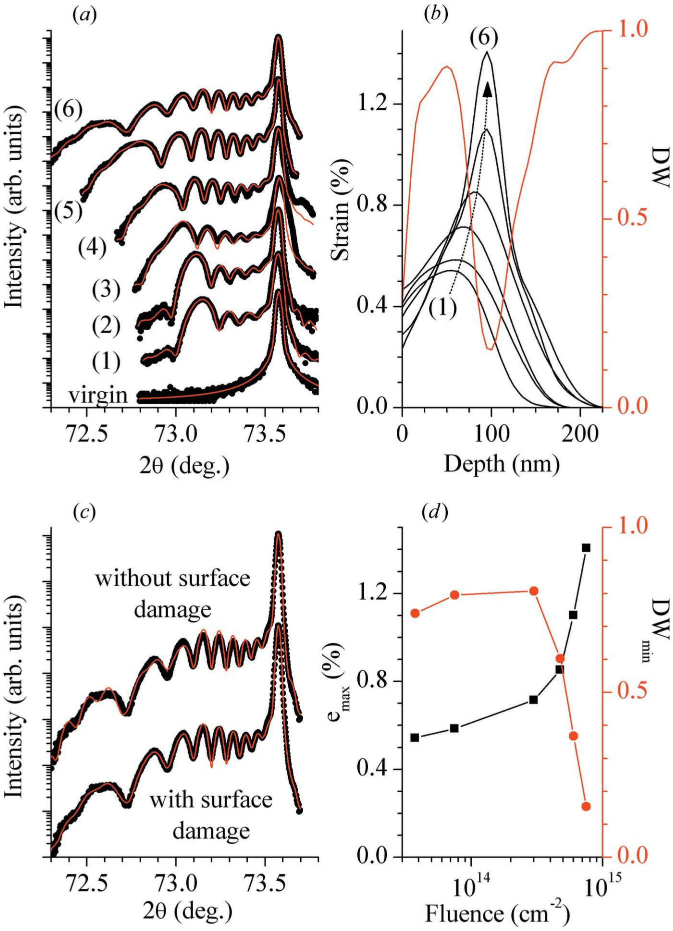

Figure 4

(*a*) θ–2θ scans recorded in the vicinity of the (400) reflection of the virgin and implanted YSZ single crystals. Black circles: experimental data; red line: simulation. The labels (1)–(6) indicate the corresponding samples. The curves are shifted vertically for clarity. (*b*) Strain profiles corresponding to samples 1–6 (black lines, left axis). The arrow indicates the evolution for increasing fluence. The Debye–Waller profile corresponding to sample 6 is also given (red line, right axis). (*c*) Influence of the surface damage on the simulations corresponding to sample 6 (black circles: experimental data; red line: simulation). The curves are shifted vertically for clarity. Neglecting surface damage clearly deteriorates the quality of simulation. (*d*) Evolution of the maximum strain, $e_{\rm max}$ (black squares, left axis), and the minimum Debye–Waller factor, DW$_{\rm min}$ (red circles, right axis), as a function of the ion fluence. The solid lines are guides to the eye. Increasing the ion fluence increases both the lattice strain and the lattice damage.

The diffraction curves corresponding to samples 1–4 have been simulated using a strain profile comprising five (sample 1) or six (samples 2–4) nonzero B-splines and a single strain/Debye–Waller proportionality factor. This latter feature implies that the lattice damage is directly related to the lattice strain, and it hence follows the same trends as those (i–iii) mentioned above for the lattice strain. Samples 5 and 6 necessitated a strain profile made of eight and ten nonzero B-splines, respectively. Moreover, in these latter cases the simple assumption that the lattice damage is related to the lattice strain did not allow the diffraction curves to be simulated. We therefore introduced an independent DW profile based on B-spline functions [similarly to the procedure implemented for the strain profile, equation (1)]. The B-spline weights corresponding to the strain profile and to the DW profile were refined independently so that the total number of fitting parameters were 16 and 20 for samples 5 and 6, respectively. With this modification, it turned out that the lattice damage is still related to the lattice strain, but it also develops close to the surface. This is illustrated in Fig. 4(*b*) (for clarity we only show the DW curve corresponding to sample 6). Actually, the position of the DW minimum (*i.e.* maximum lattice damage) clearly coincides with the position of the maximum strain, but there is an additional 25 nm-thick surface layer where the DW factor ranges between 0.3 and 0.8. In order to assess the relevance of this surface damage, we compared the simulations obtained with and without (*i.e.* the DW factor is kept equal to 0.8 in the corresponding region) surface damage (see Fig. 4*c*). The simulation in this latter case clearly fails to reproduce the experimental data, especially in the low-angle region. Hence it can be concluded that, for the highest fluences, lattice damage develops not only in the core of the implanted region but also close to the surface.

Finally, in Fig. 4(*d*) we plot the evolution of the maximum lattice strain ($e_{\rm max}$) and the maximum lattice damage (given by the minimum value of the DW factor) in the implanted region as a function of the ion fluence. In the case of lattice strain we recover the behavior already observed for this material (Debelle *et al.*, 2010), *i.e.* the lattice strain first slowly increases between 3.75×10^{13} and 3×10^{14} cm^{-2} and then strongly increases between 3×10^{14} and 7.5×10^{14} cm^{-2}. The evolution of the maximum lattice damage follows a similar behavior to the maximum strain. In a first step, it remains roughly constant and, as the strain starts to significantly increase, the DW factor strongly decreases. For the highest fluence studied here (7.5×10^{14} cm^{-2}), the region corresponding to the highest lattice strain is significantly damaged (DW = 0.15). Above 7.5 × 10^{14} cm^{-2} (5 × 10^{15} cm^{-2}, data not shown here; see Debelle *et al.*, 2010) a significant strain relaxation is observed, associated with a pronounced decrease of the XRD intensity emanating from the implanted region (which hinders its simulation). This weakening of the XRD intensity is very likely due to the growth of the highly damaged region towards both sides of the damage peak. In other words, the region with a low DW factor extends over a larger depth range instead of being confined within the highly strained region. At higher fluences (5 × 10^{16} cm^{-2}) the amorphization (corresponding to DW = 0) of the implanted region was evidenced by transmission electron microscopy (Vincent *et al.*, 2008). The simulations presented in this work show that this amorphization is not an abrupt process. On the contrary, the lattice damage increases in magnitude and extends in size until a complete amorphization of the implanted region is reached.

5. Conclusions

In order to determine the strain profiles (and the associated damage profiles) in implanted single crystals from X-ray diffraction data, we have developed a simulation procedure based on the dynamical theory of diffraction, including a B-spline description of the strain profile and making use of the generalized simulated annealing algorithm. This algorithm allows one to find the global minimum of the error function in a few hundred computing steps (*i.e.* a few seconds or tens of seconds depending on the number of parameters).

The proposed procedure has been applied to the study of Cs-implanted YSZ single crystals. We have shown that Cs implantation gives rise to an inhomogeneous lattice strain and lattice damage distribution in the direction perpendicular to the crystal surface. As the ion fluence increases, the magnitude of the strain in the implanted region increases, the width of the strained region increases and the position of the maximum strain is shifted towards higher depths. Since the lattice damage is related to lattice strain, similar conclusions hold for the lattice damage, except for the two highest investigated fluences (6 × 10^{14} and 7.5 × 10^{14} cm^{-2}) where lattice damage also develops close to the surface.

The simulation procedure developed in this work is obviously not limited to implanted YSZ but can be efficiently used for the analysis of any type of single-crystal or epitaxial heterostructure exhibiting an inhomogeneous strain distribution.

AD would like to thank Frédérico Garrido, Lionel Thomé and Alain Declémy for fruitful scientific discussions. The following free open-source softwares have been used during the course of this work: the GNU/Linux–Ubuntu operating system, the *OpenOffice.org* software suite (http://www.openoffice.org/) and the Python programming language (associated with the NumPy/SciPy and MatPlotLib libraries). The corresponding developers and communities are gratefully acknowledged.

References

Alemany, P. A. & Zanette, D. H. (1994). *Phys. Rev. E*, **49**, R956–R958.

Bartels, W. J., Hornstra, J. & Lobeek, D. J. W. (1986). *Acta Cryst.* A**42**, 539–545.

Boulle, A., Conchon, F. & Guinebretière, R. (2009). *J. Appl. Cryst.* **42**, 85–92.

Boulle, A., Masson, O., Guinebretière, R. & Dauger, A. (2003). *J. Appl. Cryst.* **36**, 1424–1431.

Brouers, F., Sotolongo-Costa, O. & Weron, K. (2004). *Physica A*, **344**, 409–416.

Correia, E. R., Nascimento, V. B., de Castilho, C. M. C., Esperidiao, A. S. C., Soares, E. A. & de Carvalho, V. E. (2005). *J. Phys. Condens. Matter*, **17**, 1–16.

Debelle, A. & Declémy, A. (2010). *Nucl. Instrum. Methods Phys. Res. Sect. B*, **268**, 1460–1465.

Debelle, A., Declémy, A., Vincent, L., Garrido, F. & Thomé, L. (2010). *J. Nucl. Mater.* **396**, 240–244.

Diaz, B., Abramof, E., Castro, R. M., Ueda, M. & Reuther, H. (2007). *J. Appl. Phys.* **101**, 103523.

Emoto, T., Akimoto, K., Ito, K., Ghatak, J. & Satyam, P. V. (2006). *e-J. Surf. Sci. Nanotechnol.* **4**, 25–31.

Geman, S. & Geman, D. (1984). *IEEE Trans. Patt. Anal. Mach. Int.* **6**, 721–741.

Gong, W. L., Lutze, W. & Ewing, R. C. (2000). *J. Nucl. Mater.* **277**, 239–249.

Hironaka, Y., Yazaki, A., Saito, F., Nakamura, K. G., Takenaka, H. & Yoshida, M. (2000). *Appl. Phys. Lett.* **77**, 1967–1969.

Kirkpatrick, S., Gelatt, C. D. & Vecchi, M. P. (1983). *Science*, **220**, 671–680.

Klappe, J. G. E. & Fewster, P. F. (1994). *J. Appl. Cryst.* **27**, 103–110.

Kriven, W., Fraser, M. W. L. & Kennedy, S. W. (1982). *Science and Technology of Zirconia*, edited by A. H. Heuer & L. W. Hoobs. Colombus: The American Ceramic Society.

Leclerc, S., Declémy, A., Beaufort, M. F., Tromas, C. & Barbot, J. F. (2005). *J. Appl. Phys.* **98**, 113506.

Lemes, M. R., Zacharias, C. R. & Dal Pino, A. Jr (1997). *Phys. Rev. B*, **56**, 9279–9281.

Metropolis, N., Rosenbluth, A. W., Rosenbluth, M. N., Teller, A. H. & Teller, E. (1953). *J. Chem. Phys.* **21**, 1087–1092.

Milita, S. & Servidori, M. (1995). *J. Appl. Cryst.* **28**, 666–672.

Moret, M. A., Pascutti, P. G., Bisch, P. M. & Mundim, K. C. (1998). *J. Comput. Chem.* **19**, 647–657.

Penna, T. J. P. (1995). *Phys. Rev. E*, **51**, R1–R3.

Pietsch, U., Holý, V. & Baumbach, T. (2004). *High-Resolution X-ray Scattering – From Thin Films to Lateral Nanostructures*. New York: Springer-Verlag.

Press, W. H., Teukolsky, S. A., Vetterling, W. T. & Flannery, B. P. (2002). *Numerical Recipes in C*. Cambridge University Press.

Ratie, P. N. & Da Silva, S. (2008). *Appl. Math. Sci.* **2**, 1359–1363.

Schanze, T. (2006). *Comput. Phys. Commun.* **175**, 708–712.

Sousbie, N., Capello, L., Eymery, J., Rieutord, F. & Lagahe, C. (2006). *J. Appl. Phys.* **99**, 103509.

Szu, H. & Hartley, R. (1987). *Phys. Lett. A*, **122**, 157–162.

Takagi, S. (1969). *J. Phys. Soc. Jpn*, **26**, 1239–1253.

Taupin, D. (1964). *Bull. Soc. Fr. Minéral. Cristallogr.* **87**, 469–511.

Thomé, L., Fradin, J., Jagielski, J., Gentils, A., Enescu, S. E. & Garrido, F. (2003). *Eur. Phys. J. Appl. Phys.* **24**, 37–48.

Tsallis, C. (1988). *J. Stat. Phys.* **52**, 479–487.

Tsallis, C. & Stariolo, D. A. (1996). *Physica A*, **233**, 395–406.

Vartanyants, I., Ern, C., Donner, W., Dosch, H. & Caliebe, W. (2000). *Appl. Phys. Lett.* **77**, 3929–3931.

Vincent, L., Thomé, L., Garrido, F., Kaitasov, O. & Houdelier, F. (2008). *J. Appl. Phys.* **104**, 114904.

Wang, L. M., Wang, S. X. & Ewing, R. C. (2000). *Philos. Mag. Lett.* **80**, 341–347.

Wierzchowski, W., Wieteska, K., Graeff, W., Turos, A. & Grötzschel, R. (2005). *Vacuum*, **78**, 569–575.

Wilk, G. & Wlodarczyk, Z. (2000). *Phys. Rev. Lett.* **84**, 2770–2773.

Xiang, Y., Sun, D. Y., Fan, W. & Gong, X. G. (1997). *Phys. Lett. A*, **233**, 216–220.

Zhaoxian, Y. & Dang, M. (2003). *Thin Solid Films*, **425**, 108–112.